High quality interconnected core/shell ZnO nanorod architectures grown by pulsed laser deposition on ZnO-seeded Si substrates

Saikumar Inguva [1,*], Rajani K. Vijayaraghavan [2], Enda McGlynn[1], Jean-Paul Mosnier [1]

[1] School of Physical Sciences and National Centre for Plasma Science and Technology, Dublin City University, Glasnevin, Dublin 9, Ireland.

[2] School of Electronic Engineering and National Centre for Plasma Science and Technology, Dublin City University, Glasnevin, Dublin 9, Ireland.

***** Corresponding author

Email: Saikumar.Inguva2@mail.dcu.ie

Keywords

ZnO; interconnected nanorods; core/shell nanorods; Si wafer substrates; pulsed laser deposition; 3.331 eV in ZnO photoluminescence.

Abstract

We report the production of vertically aligned and interconnected ZnO core/shell nanorods using pulsed laser deposition (PLD) in a continuous two-step growth process. X-ray diffraction studies showed wurtzite structure and *c*-axis orientation with a high degree of verticality. Scanning electron microscopy showed a characteristic interconnection morphology between the nanorod tips uniformly present over the entire sample surface area, while transmission electron microscopy revealed crystalline core/amorphous shell architecture. Strong bands at 98.7 cm^{-1} and 437.2 cm^{-1} (wurtzite ZnO low and high non-polar E_2 modes) were the main features of the nanorod Raman spectra, again showing the high sample quality. Low-temperature PL data exhibited strong I_6 emission and structured green band showing high optical quality. Electrical studies indicated *n*-type material with ohmic behaviour. The results are discussed in the context of the advantages offered by interconnected architectures of core/shell ZnO nanostructures for various applications.

1. Introduction

Interconnected architectures of ZnO nanostructures have been attracting significant attention due to their interesting properties. Notably, such architectures enable electrical conduction throughout the deposit, without requiring a conductive substrate, and, thus, offer unique advantages for many applications. One example is of electrical conductivity-based sensors where the high surface to volume ratio of the nanorod morphology can be combined with electrical connectivity across the deposit for electrical detection of analytes [1-4]. Other applications of these structures have been studied in various fields including sensors, photovoltaics, energy storage, photodetectors, photocatalysis and photoelectrochemistry.

For gas sensor applications, Rahmani et al. [5], Ang et al. [1] and Mani et al. [6] have reported hydrothermally-grown interconnected ZnO nanowires and spray pyrolysis-grown interconnected ZnO nanoplatelets on ZnO- and/or Au-coated glass substrates, respectively. Hosseini et al. [2,7] have also reported vapour phase transport (VPT)-grown interconnected ZnO flower-like nanostructures on quartz and Au-coated SiO_2/Si (100) substrates for gas sensors. For UV sensor applications, Gedamu et al. [8] have reported flame transport-synthesised interconnected ZnO nanotetrapod networks on quartz and SiO_2/Si (100) substrates. For glucose sensor applications, Wei et al. [9] have reported hydrothermally-grown interconnected ZnO nanorod/Au hybrid nanocomposites. For photovoltaic applications, Sudhagar et al. [3] and Tanveer et al. [4] have reported wet chemically-synthesised interconnected ZnO nanorods on fluorine-doped tin oxide (FTO) substrates and interconnected ZnO nanofibers on ITO-coated glass substrates, respectively.

For energy storage applications, Qin et al. [10] have reported partly sacrificed template-grown interconnected ZnO-Fe_2O_3 flower-like nanostructures on copper (Cu) foils while Fang et al. [11] have reported hydrothermally and chemical bath deposition (CBD)-grown interconnected ZnO/NiO core/shell nanorods on nickel (Ni) foils for lithium (Li) ion batteries. In terms of UV photodetector applications, Yingying et al. [12] and Rajabi et al. [13] have reported hydrothermally- and VPT-grown interconnected ZnO nanorods on ZnO-seeded Si and porous Si substrates, respectively. In terms of photocatalysis and photoelectrochemistry applications, Wang et al. [14] and Li et al. [15] have reported CBD-grown interconnected ZnO nanoflowers and nanorods, respectively. This brief review together with other works [16-22] highlight the interest in, and demand for production, of interconnected ZnO architectures.

Core/shell structured nanorods have also been generating interest because of their enhanced physical, chemical, structural and opto-electrical properties via modification of the nanostructure surfaces, e.g. [23, 24]. ZnO-based core/shell nanostructures have been studied for many applications including gas sensors [25], solar cells [26], energy storage and supercapacitors [27, 28]. In a previous report, Inguva et al. [29] have described a specific method of catalyst-free pulsed laser deposition (PLD) to produce self-organised ZnO core/shell nanorods on ZnO-seeded Si (100) substrates.

Based on the above reviews, it would seem interesting to combine ZnO nanorod interconnected and core/shell structures into a single architecture that would avail of the best features of both types of morphology. In this work, we report the production of high quality interconnected core/shell architectures of vertically aligned ZnO nanorods using catalyst-free

PLD on ZnO-seeded Si substrates as part of a continuous two step growth process. We investigate the structural, surface morphology, luminescence and electrical properties of these interconnected core/shell nanorods. Potential applications for such nanorod architectures are also suggested.

2. Experimental details

Interconnected ZnO core/shell nanorods were grown on ZnO-seeded Si (100) substrates using PLD. A high power, Q-switched, Nd:YAG laser with the following features was used: pulse width (6 ns), output wavelength (266 nm), repetition rate (10 Hz), laser pulse energy (110 mJ) and average fluence (~ 1.5 J/cm^2). The distance between target (a 99.99% pure ZnO sintered ceramic target purchased from PI-KEM) and substrate (cleaved 1 cm × 2 cm pieces of Si (100) wafer) was kept constant at 5 cm. Prior to deposition, the substrates were cleaned for 15 minutes in both acetone and isopropyl alcohol.

Before deposition, the substrates were heated to 900 °C for 30 minutes for surface cleaning i.e. removal/vaporisation of hydrocarbon contaminants and was then cooled down to 450 °C. In the first stage of the growth process a ZnO seed layer was deposited on the Si substrates by PLD using 5000 laser shots (~ 80 nm thickness) at a substrate temperature of 450 °C in an ambient O_2 pressure of 100 mTorr. After the seed layer growth, the substrate temperature was increased to 700 °C at a rate of ~ 12.5 °C /min and then cooled to 150 °C at a rate of ~ 9 °C /min for a crystalline seed layer. In the second stage, the interconnected ZnO core/shell nanorods were prepared using the same PLD apparatus on the ZnO-seeded Si substrates using 40000 laser shots (~ 1.2 μm nanorod length) at a substrate temperature of 800 °C in an ambient O_2 pressure of 600 mTorr. After this

nanorods deposition step, the substrate temperature was cooled to 150 °C at a rate of ~ 8.6 °C /min (see [29] for further details). A number of growth runs were performed in the same conditions and the same nanorod architectures were obtained in each case, confirming process reproducibility. The rationale for using these growth parameters (substrate temperatures and oxygen pressures) is based on our previous investigations [30]. For example, a 450 °C growth temperature for the seed layer provides a better crystalline substrate compared with 100 °C and 300 °C growth temperatures. Furthermore, growth parameters such as a substrate temperature of 800 °C and an oxygen pressure of 600 mTorr were found to yield the best morphology in terms of a uniform nanorod deposit with sharp and faceted nanorod tips, no cracks in the deposit, and minimal non-columnar growth and merging of columns [30].

The structural characteristics were investigated by 2θ-ω x-ray diffraction scans (XRD, Bruker AXS D8 Advance). The surface morphologies and nanostructures were studied by scanning electron microscopy (SEM, Carl-Zeiss EVO series) and transmission electron microscopy (TEM and HR-TEM, FEI Technai G^2 S-Twin, operating voltage of 200 kV). Low-temperature (13 K) PL spectra were recorded using a 325 nm He-Cd laser excitation with a 1 m model SPEX 1704 monochromator. Raman spectra were measured at room temperature using a Jobin Yvon Horiba LabRAM 800 spectrometer with a 488 nm Ar^+ laser excitation source (laser spot size ~ 1 μm), focused through an 100 × microscope objective. The electrical properties were studied using a commercial four point probe/Hall effect instrument (Accent HL5500). In the four point probe system, the four probes were placed directly onto the sample surface in the Van der Pauw configuration, at the four corners

of a rectangular shaped sample. No extra contacts were deposited and/or soldered on the samples for these measurements. The Hall effect measurements were performed at a fixed magnetic field of 0.51 T under atmospheric pressure and room temperature conditions.

3. Results and discussions

3.1 Structural properties

Figure 1 shows the 2θ-ω XRD scans for both the ZnO nanorod samples and a *c*-plane terminated ZnO single crystal wafer (Tokyo Denpa). A dominant ZnO (002) reflection was seen at $2\theta \approx 34.4^{o}$ for both samples, corresponding to the ZnO (002) reflection. A weaker ZnO (004) reflection was also observed for both samples at $2\theta \approx 72.7^{o}$. No other ZnO related peaks were observed in the XRD data.

The ZnO *c*-axis lattice spacing and crystallite size values deduced from the nanorod sample (002) peak angular position (34.4^{o}) and FWHM (0.205^{o}) values were 0.519 nm and 38.7 nm, respectively. The crystallite size was calculated using Scherrer equation taking into account instrumental broadening effects, see e.g. [31]. The *c*-plane lattice spacing value of the nanorod sample (0.519 nm) is very close to that of the ZnO single crystal wafer (0.520 nm), indicating good crystalline quality of the nanorods and small residual stress along the c-axis direction. The inset of Figure 1 shows the rocking curve (RC) for the (002) reflection from the two samples. The FWHM of the RC for the interconnected core/shell nanorods is 0.86^{o}, which also indicates high crystalline quality in the vertically aligned nanorods.

3.2 Morphology studies

The nanorods morphology were studied by SEM, TEM and HR-TEM. Figure 2 (a, b) show SEM images of the nanorods at tilt angles 0º and 70º. The nanorod tips are clearly interconnected, and this morphology appears very uniform over the sample surface. The average nanorod length was ~ 1.2 μm. The SEM images confirm the nanorods verticality, as previously deduced from XRD observations and also show they are densely packed with a very uniform interconnection morphology.

Further details concerning the interconnected core/shell nanorod structure was revealed using TEM and HR-TEM. Sample regions containing hundreds of nanorods were mechanically removed from the Si substrate with the help of a blade and mounted on a 300 mesh TEM grid for analysis. The TEM data in Figure 2(c) clearly shows the core/shell architectures of these interconnected nanorods while the HR-TEM data in Figure 2(d) confirms the crystalline (cr)-ZnO/amorphous (am)-ZnO core/shell structure, where ZnO crystalline or amorphous materials are observed in the core or the shell regions, respectively. Defect sites at the interface of the core/shell regions were also observed (see Figure 2(d)).

The lower laser pulse energy of 110 mJ and fluence on target of ~ 1.5 J/cm^2 used for growth of the interconnected core/shell nanorods, compared to the value of 150 mJ reported in [29], may play a role in the formation of the newly observed interconnection morphology, though further investigation of this hypothesis is required. Previous works by Wang [32] and Guo et al. [33] have shown significant effects of laser pulse energy on nanorod morphology. Overall however, the details of the entire growth process, including the exact sequence of substrate temperature changes, the laser pulse energy, as well as the tendency of ZnO towards

self-organisation [34], will all influence the ZnO growth mode and kinetics [35] in a complex manner which eventually leads to the formation of an interconnected crystalline core/amorphous shell architecture for the ZnO nanorods.

3.3 Raman spectroscopy studies

Strong and sharp bands at 98.7 cm^{-1} and 437.2 cm^{-1} were observed in the Raman spectra for the nanorod sample (Figure 3). These bands are attributed to the non-polar E_2 vibrational modes of the wurtzite phase of ZnO [36-38]. The E_2 (low) mode is associated with the vibration of the heavy Zn sub-lattice, while the E_2 (high) mode mainly involves the oxygen atoms [39]. Weaker peaks at around 376 cm^{-1} and 330 cm^{-1} are attributed to the A_1 transverse optical mode and the second order Raman process (E_2(high)-E_2(Low)), respectively [40,41]. We have also measured the Raman spectrum of the *c*-axis oriented ZnO single crystal wafer. Slight red (~ 0.4 cm^{-1}) and blue (~ 1 cm^{-1}) shifts for the E_2 (high) band and E_2 (low) bands of the nanorods were observed in respect of the bulk wafer values of 437.6 cm^{-1} and 97.8 cm^{-1}, respectively. This may be attributed to the small residual stress effects of the nanorod tip interconnections on the lattice structure (see section 3.1). The Raman studies confirm the wurtzite phase with a high lattice structure quality for the interconnected ZnO core/shell nanorods.

3.4 Optical properties

The low-temperature PL spectra (Figure 4(a)) for the ZnO nanorods show the free exciton (FE), surface exciton (SE) and strong I_6 bound exciton (BX) emission lines at ~ 3.372 eV, 3.367 eV and 3.361 eV, respectively. This reflects the high optical quality of the nanorods. Additionally, a distinctive emission feature is also observed at 3.331 eV photon

energy in Figure 4(a). Detailed studies [29,42] have shown convincingly that the 3.331 eV band is attributable to electron-hole recombination at structural defects associated with the core/shell boundary interface region. Since the present interconnected cr-ZnO/am-ZnO core/shell nanorods exhibit a similar defect structure at the core-shell interfacial regions, the same assignment is proposed for the 3.331 eV emission band. In the visible region, a clearly structured green band with zero-phonon line (ZPL) and its several longitudinal optical (LO) phonon replicas are observed in Figure 4(b). Such features are attributed to copper impurities in the ZnO lattice [43].

3.5 Electrical properties

Since the present core/shell nanorods are interconnected, we have performed four point probe measurements in order to investigate their electrical resistivity. In Figure 5, the linear behaviour of the I-V plot shows that the interconnected nanorods possess ohmic character. The resistivity of the deposit was measured to be 195 Ω cm with a carrier concentration of 2.1×10^{15} cm^{-3} and Hall mobility 49.4 cm^2 V^{-1} s^{-1}. This resistivity value is linked to the high oxygen pressure value of 600 mTorr used during the nanorods growth sequence [31,35,44]. It has been shown [35,44] that if the oxygen pressure is high during deposition, then the concentration of oxygen vacancies is reduced, leading to a decrease in carrier concentration and hence an increase in resistivity. The resistivity of 195 Ω cm corresponds to a sheet resistance of 1.5 MΩ/sq and resistance of ~ 3 MΩ, which would be acceptable for device operation. Similar resistance values in the range ~ 0.01-100 MΩ for interconnected ZnO nanorods and nanoplatelets films were used in gas sensor applications [2,6]. For comparison, we also measured the electrical resistivity, carrier concentration and

Hall mobility of the previously reported core/shell nanorods and the values were about 360 Ω cm, 6.5×10^{14} cm^{-3} and 13.4 cm^2 V^{-1} s^{-1}, respectively. As expected, the resistivity of the present interconnected core/shell nanorods was lower and, most importantly, their Hall mobility significantly higher due to the electrically interconnected architecture of these nanorods.

4. Conclusions

We have grown interconnected architectures of crystalline ZnO/amorphous ZnO core/shell nanorods by catalyst-free PLD on Si substrates in a continuous growth process. These interconnected core/shell nanorods show good crystalline quality with a high degree of verticality and excellent uniformity, as well as excellent optical quality. The samples electrical characteristics would indicate their suitability for a variety of applications, including in electrical conductivity-based sensing where they could enable electrical conduction throughout the deposit without requiring a conductive substrate, thus offering advantages whereby the high surface to volume ratio of the nanorod morphology is combined with electrical connectivity across the deposit. In addition to the sensing applications, the excellent optical quality, verticality, uniformity, and closely packed nanorod surfaces mean that these interconnected core/shell nanorods could also potentially be used in other applications such as energy storage, field emission, UV photodetectors or photocatalysis.

Acknowledgments

S. Inguva acknowledges the award of a postgraduate studentship from INSPIRE (Integrated Nanoscience Platform for Ireland). This INSPIRE-funded work was conducted under the framework of the Irish Government's Programme for Research in Third Level Institutions, Cycle 5, National Development Plan 2007-2013, with the assistance of the European Regional Development Fund. All authors gratefully acknowledge Mr. Sandeep Kumar Marka and Dr. Vadali.V.S.S. Srikanth, University of Hyderabad, Telangana, India, for their help with TEM experiments.

References

[1] W. Ang, W. Zhao, P. Liu-Hua, L. Wei-Wei, X. Li, D. Xiao-Chen, H. Wei, Room-temperature NH_3 gas sensor based on hydrothermally grown ZnO nanorods, Chin. Phys. Lett. 28 (2011) 080702, DOI:10.1088/0256-307X/28/8/080702.

[2] Z.S. Hosseini, A. Iraji zad, A. Mortezaali, Room temperature H_2S gas sensor based on rather aligned ZnO nanorods with flower-like structures, Sens. Actuators B 207 (2015) 865–871, DOI: 10.1016/j.snb.2014.10.085.

[3] P. Sudhagar, R. Saravana Kumar, J.H. Jung, W. Cho, W. Sathyamoorthy, J. Won, Y.S. Kang, Facile synthesis of highly branched jacks-like ZnO nanorods and their applications in dye-sensitized solar cells, Mater. Res. Bull. 46 (2011) 1473–1479, DOI: 10.1016/j.materresbull.2011.04.027.

[4] M. Tanveer, A. Habib, M.B. Khan, Improved efficiency of organic/inorganic photovoltaic devices by electrospun ZnO nanofibers, Mater. Sci. Eng. B 177 (2012) 1144–1148, DOI: 10.1016/j.mseb.2012.05.025.

[5] M.B. Rahmani, M. Breedon, D. Lau, J.L. Campbell, A. Moafi, D.G. McCulloch, W. Wlodarski, K. Kalantar-Zadeh, Gas sensing properties of interconnected ZnO nanowires, Sens. Lett. 9 (2011) 929–935, DOI: 10.1166/sl.2011.1646.

[6] G.K. Mani, J.B.B. Rayappan, Novel and facile synthesis of randomly interconnected ZnO nanoplatelets using spray pyrolysis and their room temperature sensing characteristics, Sens. Actuators B 198 (2014) 125–133, DOI: 10.1016/j.snb.2014.02.101.

[7] Z.S. Hosseini, A. Mortezaali, A. Iraji zad, S. Fardindoost, Sensitive and selective room temperature H_2S gas sensor based on Au sensitized vertical ZnO nanorods with flower-like structures, J. Alloy Compd. 628 (2015) 222–229, DOI: 10.1016/j.jallcom.2014.12.163.

[8] D. Gedamu, I. Paulowicz, S. Kaps, O. Lupan, S. Wille, G. Haidarschin, Y.K. Mishra, R. Adelung, Rapid fabrication technique for interpenetrated ZnO nanotetrapod networks for fast UV sensors, Adv. Mater. 26 (2014) 1541–1550, DOI: 10.1002/adma.201304363.

[9] Y. Wei, Y. Li, X. Liu, Y. Xian, G. Shi, L. Jin, ZnO nanorods/Au hybrid nanocomposites for glucose biosensor, Biosens. Bioelectron. 26 (2010) 275–278, DOI:10.1016/j.bios.2010.06.006.

[10] L. Qin, Q. Zhu, G. Li, F. Liu, Q. Pan, Controlled fabrication of flower–like ZnO–Fe_2O_3 nanostructured films with excellent lithium storage properties through a partly sacrificed template method, J. Mater. Chem. 22 (2012) 7544–7550, DOI: 10.1039/c2jm30277b.

[11] J. Fang, Y.F. Yuan, L.K. Wang, H.L. Ni, H.L. Zhu, J.S. Gui, J.L. Yang, Y.B. Chen, S.Y. Guo, Hierarchical ZnO@NiO core–shell nanorod array as high performance anode material for lithium-ion batteries, Mater. Lett. 111 (2013) 1–4, DOI: 10.1016/j.matlet.2013.08.058.

[12] L. Yingying, C. Chuanwei, D. Xiang, G. Junshan, Z. Haiqian, Facile fabrication of UV photodetectors based on ZnO nanorod networks across trenched electrodes, J. Semicond. 30 (2009) 063004, DOI: 10.1088/1674-4926/30/6/063004.

[13] M. Rajabi, R.S. Dariani, A. Iraji Zad, UV photodetection of laterally connected ZnO rods grown on porous silicon substrate, Sens. Actuators A 180 (2012) 11–14, DOI: 10.1016/j.sna.2012.04.003.

[14] Y. Wang, X. Li, N. Wang, X. Quan, Y. Chen, Controllable synthesis of ZnO nanoflowers and their morphology-dependent photocatalytic activities, Sep. Purif. Technol. 62 (2008) 727–732, DOI: 10.1016/j.seppur.2008.03.035.

[15] Z. Li, S. Feng, S. Liu, X. Li, L. Wang, W. Lu, A three-dimensional interconnected hierarchical FeOOH/TiO_2/ZnO nanostructural photoanode for enhancing the performance of

photoelectrochemical water oxidation, Nanoscale 7 (2015) 19178–19183, DOI: 10.1039/c5nr06212h.

[16] Y.K. Mishra, S. Kaps, A. Schuchardt, I. Paulowicz, X. Jin, D. Gedamu, S. Wille, O. Lupan, R. Adelung, Versatile fabrication of complex shaped metal oxide nano-microstructures and their interconnected networks for multifunctional applications, Kona 31 (2014) 92–110, DOI: 10.14356/kona.2014015.

[17] P.X. Gao, C.S. Lao, W.L. Hughes, Z.L. Wang, Three-dimensional interconnected nanowire networks of ZnO, Chem. Phys. Lett. 408 (2005) 174–178, DOI: 10.1016/j.cplett.2005.04.024.

[18] Z. Yin, N. Chen, R. Dai, L. Liu, X. Zhang, X. Wang, J. Wu, C. Chai, On the formation of well-aligned ZnO nanowall networks by catalyst-free thermal evaporation method, J. Cryst. Growth 305 (2007) 296–301, DOI: 10.1016/j.jcrysgro.2007.04.043.

[19] M. Breedon, M.B. Rahmani, S.-H. Keshmiri, W. Wlodarski, K. Kalantar-zadeh, Aqueous synthesis of interconnected ZnO nanowires using spray pyrolysis deposited seed layers, Mater. Lett. 64 (2010) 291–294. DOI: 10.1016/j.matlet.2009.10.065.

[20] N. Yu, D. Deng, D. Yang, Y. Wang, T. Yang, ZnO interconnected network nanostructures grown on cracked GaN by the aqueous solution method, J. Alloy Compd. 505 (2010) L27–L30, DOI: 10.1016/j.jallcom.2010.06.129.

[21] K.S. Ranjith, R. Geethu, K.P. Vijayakumar, R.T. Rajendrakumar, Control of interconnected ZnO nanowires to vertically aligned ZnO nanorod arrays by tailoring the underlying spray deposited ZnO seed layer, Mater. Res. Bull. 60 (2014) 584–588, DOI: 10.1016/j.materresbull.2014.08.009.

[22] L. Chen, R. Yang, X. Guo, Q. Kong, T. Yang, K. Jiao, A Novel three-dimensional interconnected graphene- zinc oxide nanowall via one-step co-electrochemical deposition, Mater. Lett. 138 (2015) 124–127, DOI: 10.1016/j.matlet.2014.09.107.

[23] S.K. Panda, A. Dev, S. Chaudhuri, Fabrication and luminescent properties of *c*-Axis oriented ZnO-ZnS core-shell and ZnS nanorod arrays by sulfidation of aligned ZnO nanorod arrays, J. Phys. Chem. C 111 (2007) 5039–5043, DOI: 10.1021/jp068391c.

[24] M. Krishnaveni, S. Devadason, Improved opto-electrical behaviour of ZnO/C_{60} core/shell type organic-inorganic heterostructure, Superlattices Microstruct. 77 (2015) 91–100, DOI: 10.1016/j.spmi.2014.10.036.

[25] W. Kim, M. Baek, K. Yong, Fabrication of ZnO/CdS, ZnO/CdO core/shell nanorod arrays and investigation of their ethanol gas sensing properties, Sens. Actuators B 223 (2016) 599–605, DOI: 10.1016/j.snb.2015.09.158.

[26] H.Y. Chao, J.H. Cheng, J.Y. Lu, Y.H. Chang, C.L. Cheng, Y.F. Chen, Growth and characterisation of type-II ZnO/ZnTe core-shell nanowire arrays for solar cell applications, Superlattices Microstruct. 47 (2010) 160–164, DOI: 10.1016/j.spmi.2009.07.005.

[27] W. Ma, Q. Shi, H. Nan, Q. Hu, X. Zheng, B. Geng, X. Zhang, Hierarchical ZnO@MnO2@PPy ternary core–shell nanorod arrays: an efficient integration of active materials for energy storage, RSC Adv. 5 (2015) 39864–39869, DOI: 10.1039/c5ra06765k.

[28] C. Yuan, H. Lin, H. Lu, E. Xing, Y. Zhang, B. Xie, Electrodeposition of three-dimensional ZnO@MnO_2 core-shell nanocables as high-performance electrode material for supercapacitors, Energy 93 (2015) 1259–1266, DOI: 10.1016/j.energy.2015.09.103.

[29] S. Inguva, S.K. Marka, R.K. Vijayaraghavan, E. McGlynn, V.V.S.S. Srikanth, J.-P. Mosnier, Crystalline ZnO/amorphous ZnO core/shell nanorods: self-organized growth, structure, and novel luminescence, J. Phys. Chem. C 119 (2015) 4848−4855, DOI: 10.1021/jp511783c.

[30] E. McCarthy, Growth of zinc oxide nanowires for field emission applications. PhD thesis, Dublin City University, Dublin 9, Ireland, January, 2013, pp. 151-161.

[31] S. Inguva, R.K. Vijayaraghavan, E. McGlynn, J.-P. Mosnier, Highly transparent and reproducible nanocrystalline ZnO and AZO thin films grown by room temperature pulsed-laser deposition on flexible Zeonor plastic substrates, Mater. Res. Express 2 (2015) 096401, DOI: 10.1088/2053-1591/2/9/096401.

[32] Y. Wang, Self-assembled nanorods and nanowires from oxide functional materials grown by pulsed laser deposition. PhD thesis, The University of Birmingham, Birmingham, B15 2TT, United Kingdom, June, 2014, pp. 169–181.

[33] R. Guo, J. Nishimura, M. Matsumoto, M. Higashihata, D. Nakamura, T. Okada, Density-controlled growth of ZnO nanowires via nanoparticle-assisted pulsed-laser deposition and their optical properties, Jpn. J. Appl. Phys. 47 (2008)741–745, DOI: 10.1143/JJAP.47.741.

[34] A. Waag, Growth, in: R. Hull, C. Jagadish, R.M. Osgood Jr., J. Parisi, Z. Wang, H. Warlimont (Eds.), Zinc oxide-from fundamental properties towards novel application, Springer, Berlin, Germany, 2010, pp. 66–67.

[35] R. Eason, Pulsed laser deposition of thin films: applications-led growth of functional materials, Wiley, Hoboken, New Jersey, 2007, pp. 177–180, pp. 240–244, and pp. 268–282.

[36] V. Gupta, P. Bhattacharya, Yu.I. Yuzuk, K. Sreenivas, R.S. Katiyar, Optical phonon modes in ZnO nanorods on Si prepared by pulsed laser deposition, J. Cryst. Growth 287 (2006) 39–43, DOI: 10.1016/j.jcrysgro.2005.10.039.

[37] D. Polsongkram, P. Chamninok, S. Pukird, L. Chow, O. Lupan, G. Chai, H. Khallaf, S. Park, A. Schulte, Effect of synthesis conditions on the growth of ZnO nanorods via hydrothermal method, Physica B 403 (2008) 3713–3717, DOI: 10.1016/j.physb.2008.06.020.

[38] L. Liao, H.B. Lu, J.C. Li, H. He, D.F. Wang, D.J. Fu, C. Liu, W.F. Zhang, Size dependence of gas sensitivity of ZnO nanorods, J. Phys. Chem. C 111 (2007) 1900–1903, DOI: 10.1021/jp065963k.

[39] Ü. Özgür, Ya.I. Alivov, C. Liu, A. Teke, M.A. Reshchikov, S. Doğan, V. Avrutin, S.-J. Cho, H. Morkoç, A comprehensive review of ZnO materials and devices, J. Appl. Phys. 98 (2005) 041301, DOI: 10.1063/1.1992666.

[40] K.A. Alim, V.A. Fonoberov, A.A. Balandin, Origin of the optical phonon frequency shifts in ZnO quantum dots, Appl. Phys. Lett. 86 (2005) 053103, DOI: 10.1063/1.1861509.

[41] L.-L. Xing, C.-H. Ma, Z.-H. Chen, Y.-J. Chen, X.-Y. Xue, High gas sensing performance of one-step-synthesized Pd–ZnO nanoflowers due to surface reactions and modifications, Nanotechnology 22 (2011) 215501, DOI: 10.1088/0957-4484/22/21/215501.

[42] S. Inguva, C. Gray, E. McGlynn, J.-P. Mosnier, Origin of the 3.331 eV emission in ZnO nanorods: Comparison of vapour phase transport and pulsed laser deposition grown nanorods, J. Lumin. 175 (2016) 117–121, DOI: 10.1016/j.jlumin.2016.02.027.

[43] D. Byrne, F. Herklotz, M.O. Henry, E. McGlynn, Unambiguous identification of the role of a single Cu atom in the ZnO structured green band, J. Phys.: Condens. Matter 24 (2012) 215802, DOI: 10.1088/0953-8984/24/21/215802.

[44] J.H. Lee, C.-Y. Chou, Z. Bi, C.-F. Tsai, H. Wang, Growth-controlled surface roughness in Al-doped ZnO as transparent conducting oxide, Nanotechnology 20 (2009) 395704, DOI: 10.1088/0957-4484/20/39/395704.

Figure captions

Figure 1. 2θ-ω XRD scans for interconnected ZnO core/shell nanorods (black line) and ZnO single crystal wafer (blue line) (the features marked '*' are due to contaminants). The inset shows the rocking curve scans from the two samples around the ZnO (002) peak position. Inset uses the same colour scheme as in the main figure.

Figure 2. SEM (a, b), TEM (c) and HR-TEM (d) images of the interconnected cr-ZnO/am-ZnO core/shell nanorods. (a): SEM images at 0º tilt (plane view), (b): 70º tilt angles, (c): TEM image showing the core/shell architecture of the nanorod in a wider view close to the middle of the nanorod, and (d): HR-TEM image showing crystalline core and amorphous shell architecture of a nanorod at the tip. Inset of (a) shows the enlarged view of the same image.

Figure 3. Raman spectra in the range 50-450 cm^{-1} for the interconnected cr-ZnO/am-ZnO core/shell nanorods (black lines) and a ZnO single crystal wafer (blue lines). The marked peaks with '*' are Si related Raman features.

Figure 4. Low temperature (13 K) PL spectra for the interconnected cr-ZnO/am-ZnO core/shell nanorods. (a): near band edge region showing free exciton (FE), surface exciton (SE) and emission at 3.331 eV, and (b): visible region showing structured green band emission with zero-phonon line (ZPL) and its longitudinal optical (LO) phonon replicas.

Figure 5. I-V plot for the *n*-type interconnected cr-ZnO/am-ZnO core/shell nanorods.

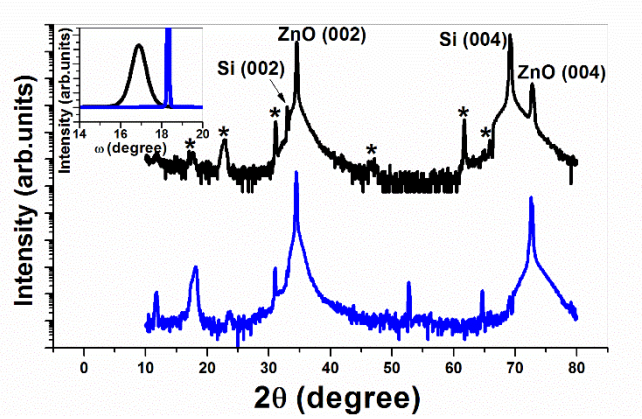
ZnO (002)
Si (004)
Si (002)
ZnO (004)
Intensity (arb.units)
2θ (degree)
ω (degree)

Figure 1

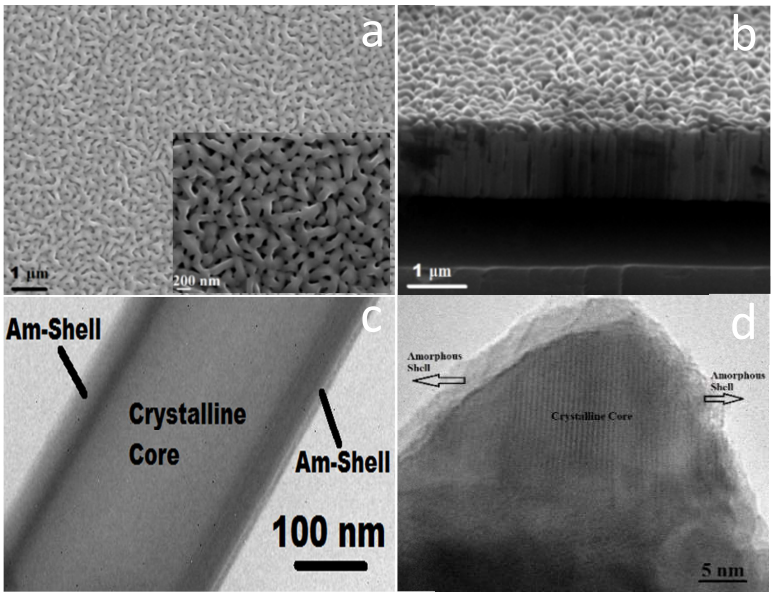
a
1 µm
200 nm
b
1 µm
c
Am-Shell
Crystalline
Core
Am-Shell
100 nm
d
Amorphous
Shell
Crystalline Core
Amorphous
Shell
5 nm

Figure 2

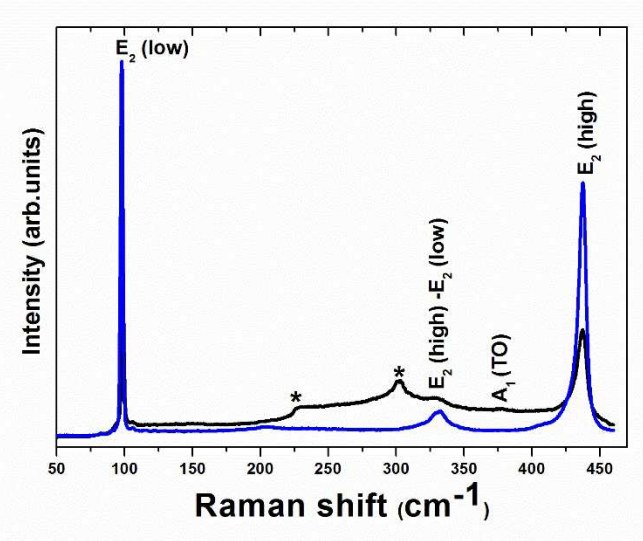
E2 (low)
E2 (high) -E2 (low)
A1 (TO)
E2 (high)
*
*
Intensity (arb.units)
50
100
150
200
250
300
350
400
450
Raman shift (cm-1)

Figure 3

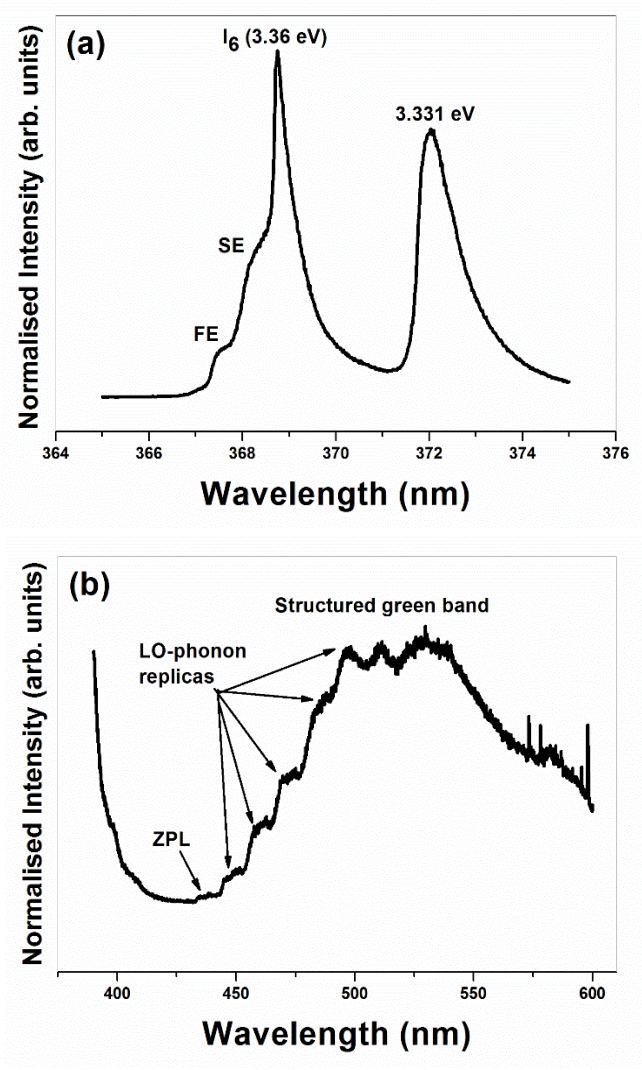
(a)
I_6 (3.36 eV)
3.331 eV
SE
FE
Normalised Intensity (arb. units)
364
366
368
370
372
374
376
Wavelength (nm)
(b)
Structured green band
LO-phonon
replicas
ZPL
Normalised Intensity (arb. units)
400
450
500
550
600
Wavelength (nm)

Figure 4

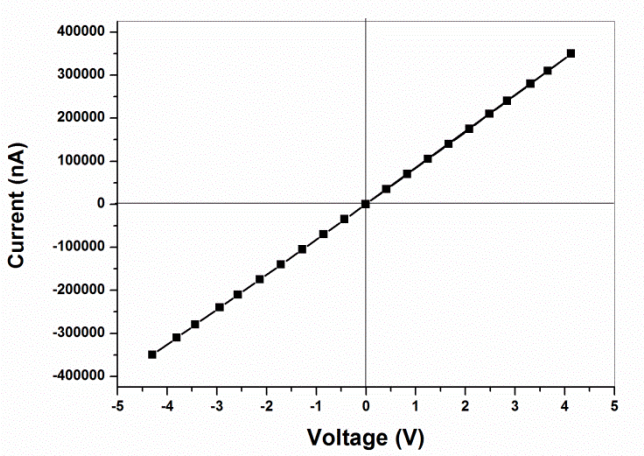
Current (nA)
400000
300000
200000
100000
0
-100000
-200000
-300000
-400000
-5
-4
-3
-2
-1
0
1
2
3
4
5
Voltage (V)

Figure 5